Nuclear Materials and Energy 26 (2021) 100864

Contents lists available at ScienceDirect

Nuclear Materials and Energy

journal homepage: www.elsevier.com/locate/nme

Simulation studies of divertor detachment and critical power exhaust parameters for Japanese DEMO design

N. Asakura [a,*], K. Hoshino [b], Y. Homma [c], Y. Sakamoto [c], Joint Special Design Team for Fusion DEMO

[a] National Institutes for Quantum and Radiological Science and Technology (QST), Naka, Ibaraki 311-0193, Japan
[b] Graduate School of Science and Technology, Keio University, Yokohama 223-8522, Japan
[c] National Institutes for Quantum and Radiological Science and Technology (QST), Rokkasho, Aomori 039-3212, Japan

ARTICLE INFO

Keywords:
Divertor
DEMO
SONIC
Simulation
Impurity seeding
Detachment

ABSTRACT

Handling of a large thermal power exhausted from the confined plasma is one of the most important issues for ITER and DEMO. A conventional divertor, which has the closed geometry similar to that of ITER and longer leg of 1.6 m, was proposed for the Japanese (JA) DEMO reactor (R_p/a_p = 8.5/2.42 m). A radiative cooling scenario of Ar impurity seeding and the divertor performance have been demonstrated by SONIC simulation, in order to evaluate the power exhaust in JA-DEMO 2014 (primary design with $P_{sep} \sim 283$ MW) and JA-DEMO with higher plasma elongation (a revised design with $P_{sep} \sim 235$ MW). The divertor operation with the peak $q_{target} \leq 10$ MWm^{-2} was determined in the low n_e^{sep} of 2–3 $\times 10^{19}$ m^{-3} under the severe conditions of reducing radiation loss fraction, i.e. $f^{*div}_{rad} = (P^{sol}_{rad} + P^{div}_{rad})/P_{sep}$, and diffusion coefficients (χ and D). The divertor geometry and reference key parameters ($f^{*div}_{rad} \sim 0.8$, $\chi = 1$ m^2/s and $D = 0.3$ m^2/s) were so far consistent with the power exhaust concepts in the n_e^{sep} range, and the revised JA-DEMO design has advantages of wider n_e^{sep} range and enough margin for the divertor operation. For either severe assumption of $f^{*div}_{rad} \sim 0.7$ or χ and D to the half value, higher n_e^{sep} operation was required for the primary design in order to control the peak $q_{target} \leq 10$ MWm^{-2}, i.e. the operation window was reduced. Applying the two severe assumptions, the divertor operation was difficult in the low n_e^{sep} range for the both designs.

1. Introduction

A steady-state DEMO fusion reactor with 1.5 GW-level fusion power (JA-DEMO 2014) has been proposed by the Joint Special Team for Demo Design in Japan [1,2]. The representative plasma parameters were evaluated by the system code (TPC) [3], i.e. plasma current (I_p): 12.3MA, toroidal magnetic field (B_t): 5.94 T, major radius (R_p): 8.5 m, minor radius (a_p): 2.42 m, plasma elongation at 95% minor radius (κ_{95}): 1.65, safety factor (q_{95}): 4.1, triangularity (δ_{95}): 0.3, and fusion power (P_{fusion}): 1.46 GW was expected by maintaining relatively high H-factor of the plasma confinement ($HH_{98(y,2)}$) at 1.3 in the Ar impurity seeding plasma ($c_{Ar}^{main} = n_{Ar}/n_e = 0.25\%$) and He concentration ($n_{He}/n_e$) of 7%. Further increase of c_{Ar}^{main} reduced P_{fusion} (and electric power generation) lower than 1.5 GW-level due to the fuel dilution as shown in Fig. 1(a) in Reference 4, and, at the same time, higher $HH_{98(y,2)}$ was required. Thus, for the primary plasma design, the radiation fraction of the main plasma normalized by the plasma heating power (P_{heat}) of 376 MW was restricted at $f_{rad}^{main} = P_{rad}^{main}/P_{heat} = 0.22$, which was lower than that of ITER ($f_{rad}^{main} = 0.33$). At the same time, large power handling of exhaust power to the SOL, i.e. $P_{sep} = 294$ MW and $P_{sep}/R_p = 35$ MWm^{-1}, was required for the divertor design.

A revised plasma design for the power handling [4] was proposed to increase κ_{95} and I_p to 1.75 and 13.5 MA for improvement of the plasma performance such as P_{fusion} and the energy confinement time (τ_E), while the plasma size, B_t and relatively high q_{95} were fixed for the steady-state plasma design. Impurity seeding could be enhanced to $c_{Ar}^{main} \sim 0.6\%$, where f_{rad}^{main} was increased to 0.41, P_{sep} was reduced to 258 MW and P_{sep}/R_p to 30 MWm^{-1}, while the high $P_{fusion} \sim 1.7$ GW and $HH_{98(y,2)} \sim 1.3$ were achieved at the same time, as shown in Table I in Reference 4. The revised plasma design (JA-DEMO higher-κ) would be appropriate for the power handling in the main plasma and divertor, and the plasma operation window was extended.

An ITER-like divertor geometry with a long leg ($L_{div} = 1.6$ m, 1.6 times longer than ITER) was proposed as a JA-DEMO divertor design

* Corresponding author at: Plasma Theory and Simulation Group, Naka Fusion Institute, QST, 801-1 Mukoyama, Naka, Ibaraki 311-0193, Japan.
E-mail address: asakura.nobuyuki@qst.go.jp (N. Asakura).

https://doi.org/10.1016/j.nme.2020.100864
Received 10 September 2020; Received in revised form 24 November 2020; Accepted 28 November 2020
Available online 7 December 2020

[4]. SONIC simulation for the revised plasma design (P_{sep} ~ 250 MW) with a large radiation fraction in the SOL and divertor, i.e. $f^{*div}_{rad} = (P^{sol}_{rad} + P^{div}_{rad})/P_{sep} \sim 0.8$, demonstrated that the peak heat load on the divertor target (q_{target}) was reduced to less than 10 MWm^{-2}, which is a guide line to prevent recrystallization at the tungsten monoblock surface of the DEMO divertor. For the next step, the divertor performance has been recently investigated under the severe heat flux conditions such as increasing P_{sep} and reducing $P^{sol}_{rad} + P^{div}_{rad}$, then the divertor operation ranges for the primary and revised DEMO plasma designs were evaluated in order to determine the power exhaust concept of the main plasma and divertor. In addition, decay length of the heat flux profile ($\lambda^{mid}_{q//}$) is not precisely predicted appropriate for the reactor size and the SOL condition. Thus, influence of narrow $\lambda^{mid}_{q//}$, i.e. smaller diffusion coefficient, on the plasma detachment was also evaluated. These studies of the divertor operation were provided for the steady-state DEMO design with suppressing the edge localized mode (ELM) activity. Influences of mitigated ELM on the plasma detachment and the target erosion will be necessary to finalize the DEMO plasma design in future.

The power exhaust scenarios for different DEMO concepts (P_{fusion} = 1–2 GW, R_p = 7–9 m) such as EU-DEMOs [5,6], CFETR[7], K-DEMO[8] and JA-DEMO have been recently developed, where P_{heat} is 2–3 times larger than that of ITER while R_p is increased 1.1–1.4 times. Therefore, the total radiation fraction in the main plasma and divertor becomes large ($f^{tot}_{rad} = (P^{main}_{rad} + P^{sol}_{rad} + P^{div}_{rad})/P_{heat} \geq 0.8$, compared to that for ITER (f^{tot}_{rad} = 0.6–0.7) [9], in order to reduce the peak q_{target} similar to or less than that of ITER. Requirements of f^{main}_{rad} and the plasma performance for the DEMO concept such as the steady-state or repeating long-pulse will determine P_{sep} and the divertor design [10]. These DEMO concepts propose some approaches: (i) EU-DEMO challenges increasing f^{main}_{rad} to handle ITER-level P_{sep}/R_p (~16 MWm^{-1}) in the divertor, (ii) JA-DEMO and CFETR challenge increasing f^{div}_{rad} (= $(P^{sol}_{rad} + P^{div}_{rad})/P_{heat}$) to handle large P_{sep}/R_p ~ 30 MWm^{-1} with the ITER-level f^{main}_{rad}, (iii) K-DEMO and EU-DEMO also challenge double null design to distribute the large P_{sep} to the upper and lower divertors. This power exhaust study in the long-leg divertor for JA-DEMO will significantly contribute to optimize the divertor size and geometry for the large P_{sep}/R_p concepts of DEMO and future power plant designs.

In this paper, the DEMO divertor design and simulation parameters are explained in Section 2. Operation boundaries of the divertor heat load under the severe exhaust power conditions and diffusion coefficients are summarized in Section 3 and 4, respectively. Critical issues of the partial detachment and impurity seeding are discussed in Section 5. Power exhaust studies for the JA-DEMO divertor design is summarized in Section 6.

2. Divertor design and simulation parameters

The long-leg divertor performance has been investigated, using SONIC simulation code [11,12]. In the SONIC simulation, most kinetic effects on the impurity ions in the original formula are handled in the impurity transport code (IMPMC), and radiation power from the Ar impurity is calculated, using the effective ionization coefficients, the line emissions from excitation and effective recombination coefficients of ADAS data (ADF11). Modelling of various drifts such as$\nabla B \times \boldsymbol{B}$ and $\boldsymbol{E} \times \boldsymbol{B}$ is not incorporated in the plasma fluid code (SOLDOR). Neutral-neutral and neutral-molecular collisions are not active in the kinetic neutral code (NEUT2D) since calculation resource is primarily spent for the impurity transport. SONIC code has been applied to investigate momentum loss at the plasma detachment, i.e. “roll-over” of the particle flux and intrinsic carbon impurity transport in JT-60U experiments [12,13].

The calculation mesh in the lower plasma area is shown in Fig. 1. The poloidal angle between the separatrix and target surface at the strike point (θ^{div}) is designed as 30° and 25° at the inner and outer targets, respectively, where the flux expansion at the inner and outer targets, i.e. $f^{div}_{exp}/sin\theta^{div}$ where $f^{div}_{exp} = (B_p/B_t)^{mid}/(B_p/B_t)^{div}$, is similar (~12). Plasma

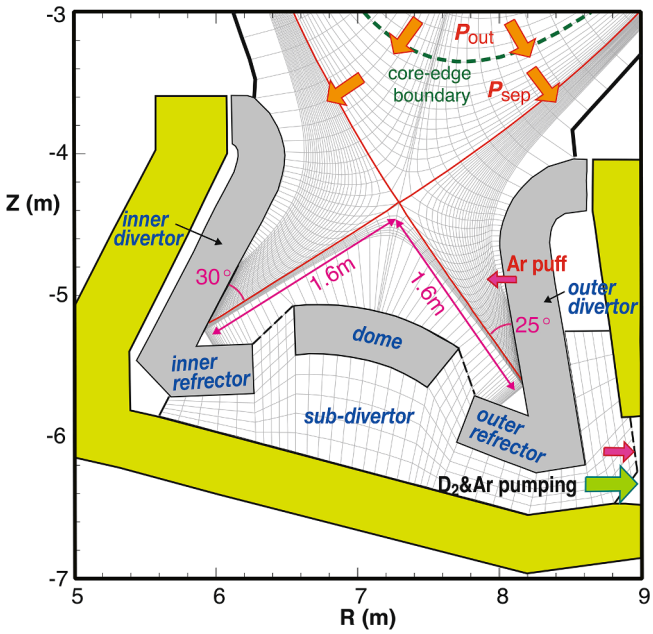

Fig. 1. Simulation mesh for SONIC calculation. Leg lengths of the inner and outer divertor are 1.6 m. Poloidal angles between the separatrix and target surface at the inner and outer strike point are 20° and 25°, respectively. Exhausted power (P_{out}) and particle (Γ_{out}) are given at the core–edge boundary (r^{mid}/a = 0.95).

transport in SOL and divertor is simulated in the flux surfaces of the outer midplane SOL radius (r^{mid}) ≤ 3.2 cm, which covers most SOL area connecting between the inner and outer targets. Reflector is installed both at the inner and outer divertors, and the poloidal angle of 60°. Exhaust power (P_{out}) and particle (Γ_{out}) from the core region are given at the core–edge boundary (the magnetic surface corresponding to r^{mid}/a_p = 0.95). Diffusion coefficients of $\chi_i = \chi_e$ = 1 m^{2}s^{-1} and D = 0.3 m^{2}s^{-1} are the same as “standard” values in the ITER simulation [14]. Deuterium (D_2) is injected near the midplane and Ar impurity puffs at the upper part of the outer target. They are exhausted from the outboard of the sub-divertor similar to ITER, instead of the bottom as shown in Reference 4. This is mainly because of reducing the fast neutron irradiation to protect the vacuum vessel, and distribution of the detachment plasma was not influenced.

Operation boundary for the divertor heat load was investigated under severe power conditions. A simple formula of the plasma heat load (q^{plasma}) is described by P_{sep}, f^{*div}_{rad}, $\lambda^{mid}_{q//}$ and geometry parameters, i.e. $q^{plasma} = P_{sep}\cdot(1\text{-}f^{*div}_{rad})\cdot(sin\theta^{div}/f^{div}_{exp})\cdot(4\pi R_p\cdot\lambda^{mid}_{q//}\cdot S^{det})^{-1}$, where power reduction in the detachment is represented by an additional factor (S^{det}). Influences of P_{sep}, f^{*div}_{rad} and diffusion coefficients on the divertor operation were systematically investigated by SONIC simulation. A series of results with increasing fuel gas puff rate from 25 to 150 Pam^{3}s^{-1} [4] were reported for the JA-DEMO higher-κ case (Case-1) of P_{out} = 250 MW and $\Gamma_{out} = 1 \times 10^{22}$ Ds^{-1}, where the total radiation power in the plasma edge ($0.95 < r^{mid}/a_p < 1$), SOL and divertor ($P^{edge}_{rad} + P^{sol}_{rad} + P^{div}_{rad}$) was fixed at 200 MW by feedback of the Ar seeding rate in the iterative calculation of SONIC. Here, Ar seeding rate was decreased with increasing fuel gas puff rate. In the gas puff scan, P^{edge}_{rad} was small (P^{edge}_{rad}/P_{out} = 0.05–0.06) and P_{sep} = 240–235 MW, thus f^{*div}_{rad} = 0.78 was slightly smaller than the input radiation fraction of $f^{inp}_{rad} = (P^{edge}_{rad} + P^{sol}_{rad} + P^{div}_{rad})/P_{out}$ = 0.80. Additional three cases were chosen as increasing the power exhaust parameter in the simple q^{plasma} formula, i.e. $P_{sep}\cdot(1\text{-}f^{*div}_{rad})$. Case-2 ($P_{out}$ = 300 MW and f^{inp}_{rad} = 0.8), Case-3 (P_{out} = 250 MW and f^{inp}_{rad} = 0.7) and Case-4 (P_{out} = 300 MW and f^{inp}_{rad} = 0.7) correspond to the power exhaust design of JA-DEMO 2014, and lower radiation cases of the JA-DEMO higher-κ and JA-DEMO 2014, respectively.

High plasma density is preferable for the plasma design and power

exhaust. On the other hand, the Greenwald density ($n^{GW} = I_p/\pi a_p^2$ [10^{20} m^{-3}, MA, m]) corresponds to 6.7 × 10^{19} and 7.3 × 10^{19} m^{-3} for the primary and revised power exhaust designs, respectively, which are lower than that of ITER (1.1 × 10^{20} m^{-3}). This is a common issue for the power exhaust for DEMOs [15], thus design values of the main plasma density (n_e^{main}) are increased to be 8.0 × 10^{19} and 8.7 × 10^{19} m^{-3}, respectively, providing the density enhancement factor of 1.2 to achieve expecting fusion power. Medium values of normalized density at the main plasma separatrix (n_e^{sep}/n^{GW}) in the H-mode plasma experiments [16,17] and "standard" ITER simulations [14] corresponded to ~ 1/3. Recent tokamak experiments with all metal plasma facing components (PFCs) and the edge ballooning stability model reported that n_e^{sep}/n^{GW} was restricted lower than critical values of 0.4–0.5 [18]. As a result, divertor operation is required in the low SOL density range such as n_e^{sep} = 2–3.5 × 10^{19} m^{-3}. In this study, operation boundaries in the low n_e^{sep} were determined for the four cases.

3. Effects of exhaust power and radiation loss on divertor operation

3.1. Radiation loss and plasma detachment

Fig. 2 (a)(b) show distributions of the radiation power density (W_{rad}) in the divertor for Case-1 at n_e^{sep} = 2.0 × 10^{19} m^{-3}. Total radiation powers in the inner and outer divertors are comparable, i.e. 79 and 82 MW, respectively. The large radiation peaks near the separatrix are maintained in the both divertor legs. In the inner divertor, large W_{rad} is seen at the upstream (50–60 cm) of the target, and T_e is decreased to ~ 1 eV over most area of the target, which we describe "full-detachment" as shown in Fig. 2(c). Total heat load (q_{target}) is evaluated by including surface recombination of the ions ($q_t^{rec} = n_i^{div} C_s^{div} E_{ion}$, where n_i^{div}, C_s^{div} and E_{ion} are ion density, sound velocity at the divertor sheath and recombination energy, respectively), radiation power load (q_t^{rad}) and neutral flux load (q_t^n), in addition to the plasma heat flux (q_t^{plasma}). The peak q_{target} of 4.2 MWm^{-2} is seen near the separatrix, mostly attributed by q_t^{rec} as shown in Fig. 2(d).

In the outer divertor, large W_{rad} is also seen at the upstream (50–60 cm) near the separatrix, where local c_{Ar}^{div} (=n_{Ar}/n_e) is increased up to 1.6% similar to that was shown in Fig. 6 (b) of Reference 4. On the other hand, it shifts towards the target at the outer flux surfaces as shown in Fig. 2(b). Here, the W_{rad} peak is smaller than 10 MWm^{-3} (lowest color bar) and located just above the target (a few cm).

The plasma detachment is produced within 12 cm near the strike-point, which we describe "partial detachment". At the same time, the plasma detachment is produced at a few 10 cm above the target, while the reduction in the density is only 1/2–1/3 at T_e and T_i of 1–2 eV in the simulation, as shown in Fig. 6(a) of Reference 4. Studies of atomic and molecular collision processes and/or enhancement of the plasma diffusion may be necessary to produce further reduction in T_e^{div} and T_i^{div}, leading to reduction in the particle flux [13,19]. The peak q_{target} of 5.6 MWm^{-2} is seen at the attached plasma area, and it is sensitive to profiles of T_e^{div}, T_i^{div} and n_e^{div}. Since T_e^{div} and T_i^{div} are increased to ~ 20 eV and the W_{rad} peak is just above the target, q_t^{plasma} and q_t^{rad} are dominant. These results suggested that the peak q_{target} can be reduced less than 10 MWm^{-2} for both inner and outer divertors even at the low n_e^{sep} of 2.0 × 10^{19} m^{-3}. The large W_{rad} and plasma detachment can be maintained in the long divertor leg.

Simulation results of the divertor performance such as reduction of the peak q_{target} were systematically summarized in ITER as a function of the averaged neutral pressure at the inner and outer openings of the dome (P_n) [9]. Neutral (D_0) and gas (D_2) pressures were comparable at the dome openings of the JA-DEMO as shown by broken lines in Fig. 1, and the total pressure at the inner and outer openings were 5.2 Pa and 3.3 Pa, respectively, for the throughput of 120 Pam^3s^{-1}. These values were comparable to the ITER operation range to reduce the peak q_{target} ≤ 10 MWm^{-2}, while smaller than the reference P_n (~10 Pa).

3.2. Divertor operation in low density SOL

The divertor detachment and peak q_{target} have been evaluated in the

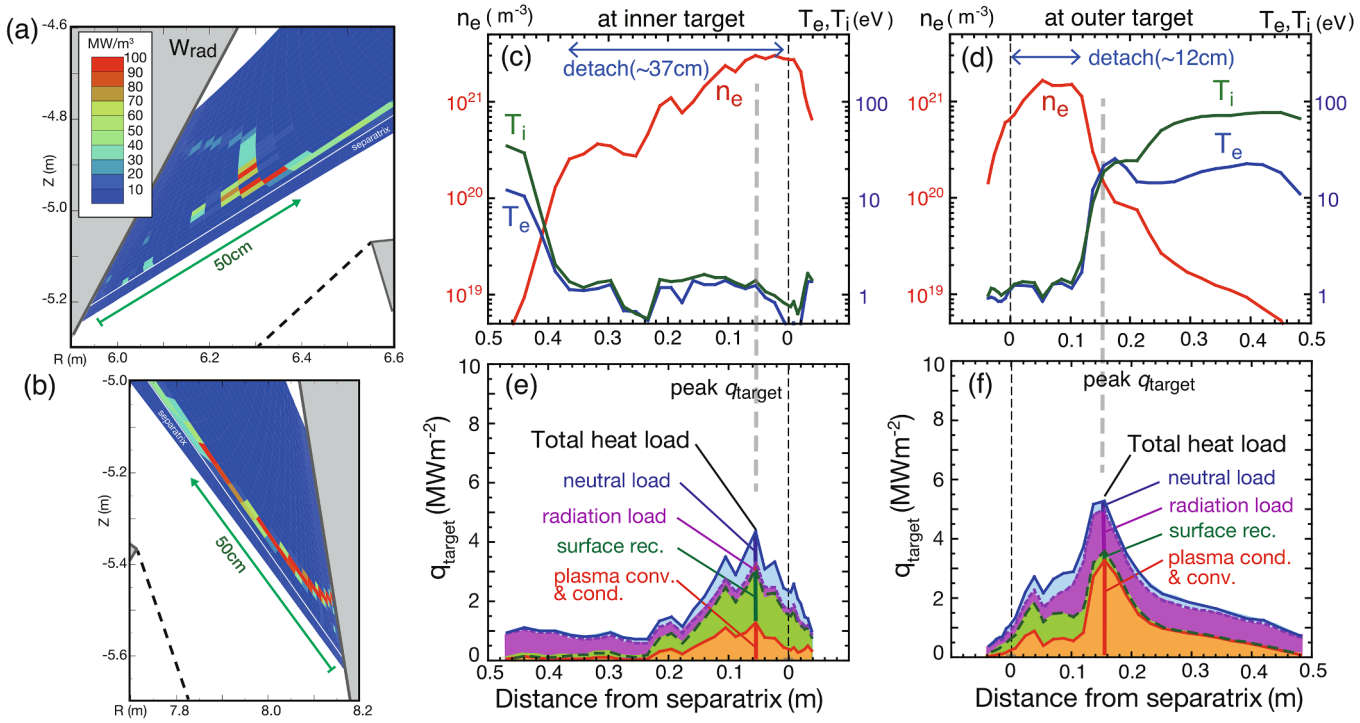

Fig. 2. (a) (b) Distributions of Ar radiation power density (W_{rad}) in the inner and outer divertors, respectively, for Case-1: n_e^{sep} = 2.0 × $10^{19}$$m^{-3}$, P_{out} = 250 MW and $P_{rad}^{edge} + P_{rad}^{sol} + P_{rad}^{div}$ = 200 MW. Profiles of (c) (e) n_e^{div}, T_e^{div} and T_i^{div}, (d) (f) integrating heat load components at the inner and outer divertor target, respectively. Width of the detachment is shown by arrows.

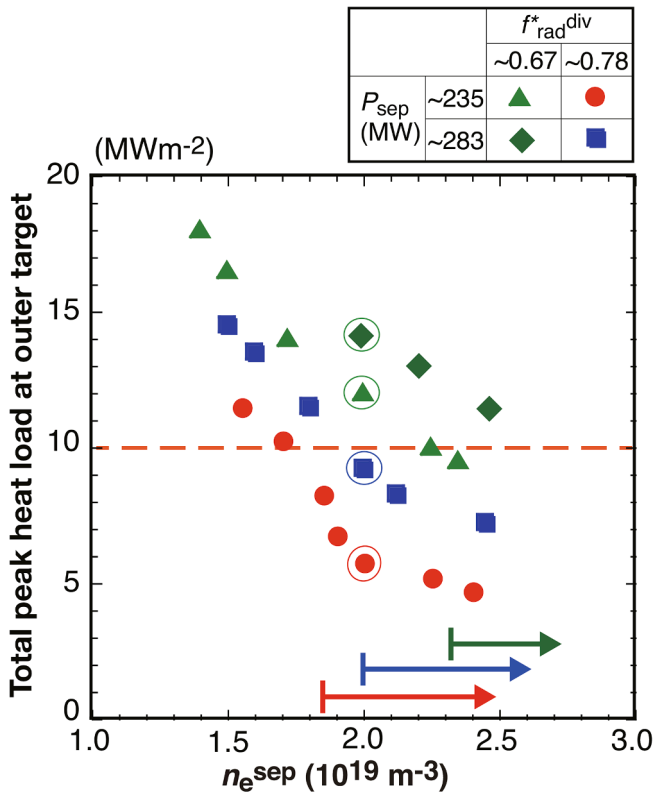

Fig. 3. Four series of peak q_{target} at the outer target for given exhaust power (P_{sep}) and radiation fraction in the SOL and divertor ($f^{*div}_{rad} = (P^{sol}_{rad} + P^{div}_{rad})/P_{sep}$) as a function of n_e^{sep}. Circles, squares, triangles and diamonds correspond to Case-1, Case-2, Case-3 and Case-4, respectively. Open circles mark the results at $n_e^{sep} = 2.0 \times 10^{19} m^{-3}$. Red, blue and green lines show n_e^{sep} ranges with peak $q_{target} \leq 10$ MWm^{-2} for Case-1, Case-2 and Case-3, respectively. (For interpretation of the references to color in this figure legend, the reader is referred to the web version of this article.)

same divertor geometry by changing the key parameters of P_{sep} and f^{*div}_{rad}, and operation boundary of the low n_e^{sep} is summarized for the four cases. Here, n_e^{sep} scan was performed by changing the gas puff and/or divertor pumping. The power to the divertor, i.e. $P_{sep}\cdot(1\text{-}f^{*div}_{rad})$, for the four cases corresponds to 50, 60, 75 and 90 MW. The outer q_{target} is generally larger than the inner q_{target}. Results of the peak q_{target} at the outer target are shown in Fig. 3. Closed circles show a series of Case-1, and the reference profiles in Fig. 2 are pointed by open circle at $n_e^{sep} = 2.0 \times 10^{19}$ m^{-3}. Closed squares, triangles and diamonds show other three series of Case-2, Case-3 and Case-4, respectively. The peak q_{target} is reduced with increasing n_e^{sep}, and it is increased with $P_{sep}\cdot(1\text{-}f^{*div}_{rad})$. Lower boundary of n_e^{sep} for $q_{target} \leq 10$ MWm^{-2} was 1.8×10^{19}, 2.0×10^{19} and 2.3×10^{19} m^{-3} for Case-1, Case-2 and Case-3, respectively. The two reference designs of Case-1 and Case-2 are acceptable in the low n_e^{sep} range of 2–3 $\times 10^{19}$ m^{-3}. Here, Case-1 will reduce the surface temperature of the W target and allow enough operation margin to the recrystallization temperature. As is expected by the lower $P_{sep}\cdot(1\text{-}f^{*div}_{rad})$, the divertor operation of the JA-DEMO higher-κ design has advantages in the low n_e^{sep} range. Higher n_e^{sep} operation ($\geq 2.3 \times 10^{19}$ m^{-3}) is acceptable for Case-3. For Case-4, further high n_e^{sep} such as larger than 2.6×10^{19} m^{-3} will be required.

Profiles of T_e^{div}, T_i^{div}, n_e^{div} at the outer target and heat load components at $n_e^{sep} = 2.0 \times 10^{19}$ m^{-3} for Case-2, Case-3 and Case-4 are compared in Fig. 4. From Case-1 to Case-4, width of the partial detachment is decreased from 12 to 7 cm. At the same time, from the detach-attach boundary to the outer region on the target ($r^{div} \sim 20$ cm), T_e^{div} and T_i^{div} are increased and n_e^{div} is decreased more significantly. The peak q_{target} is seen at ~3 cm outside of each detach-attach boundary, and the value is increased, i.e. 5.6, 9.5, 12.2 and 14.5 MWm^{-2}. The local T_e^{div} and T_i^{div} are comparable since the local n_e^{div} is still high (1.1–1.7 $\times 10^{20}$ m^{-3}) and the energy exchange rate is high, and they are also increased, i.e. 21, 25, 33 and 42 eV, respectively. It is noted that peak q_{target} at the inner target for Case-3 and Case-4 is also increased comparable to or larger than 10 MWm^{-2} due to increase of the ion flux and q_t^{rec}, while T_e^{div} and T_i^{div} are 1–2 eV. In the further outer region on the outer target ($r^{div} \geq$ 20 cm), T_e^{div} and T_i^{div} are increased with $P_{sep}\cdot(1\text{-}f^{*div}_{rad})$ from 20 eV to several 10 eV and from several 10 eV to 100–200 eV, respectively, and

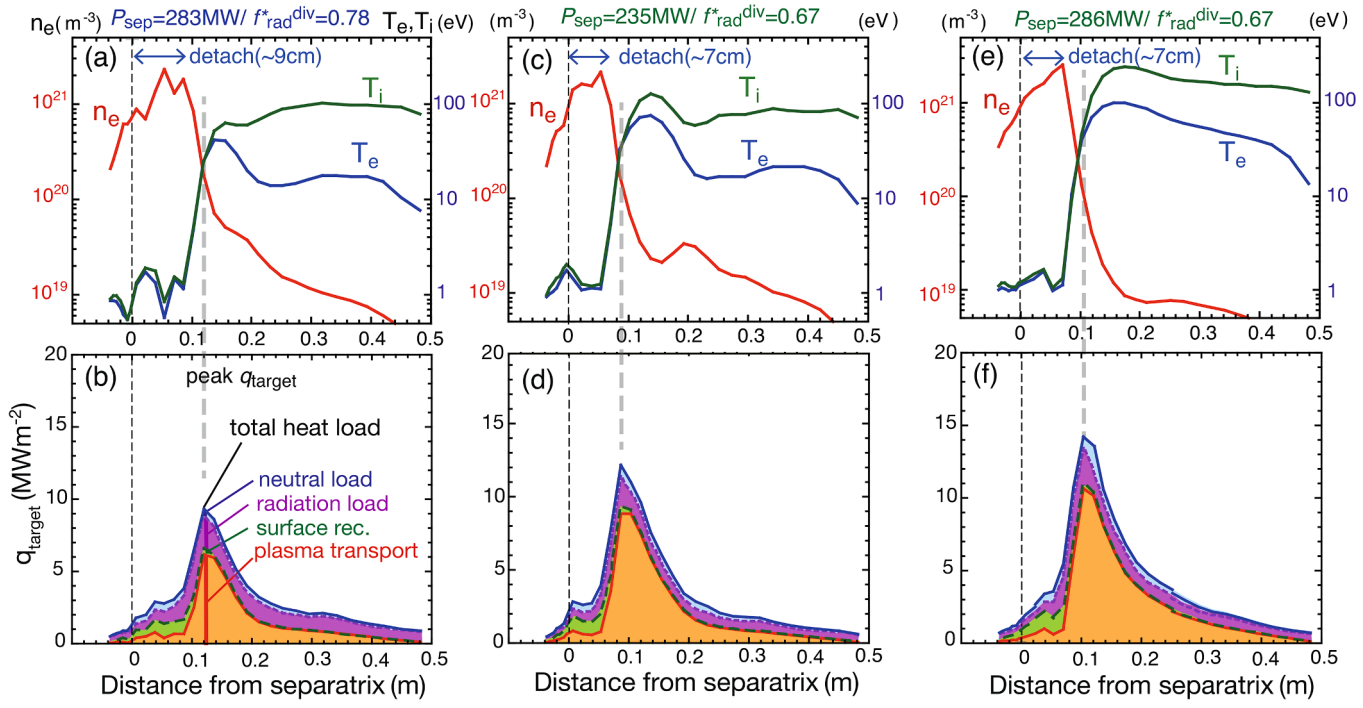

Fig. 4. Upper shows profiles of T_e^{div}, T_i^{div}, n_e^{div}, and lower shows profiles of q_{target} and integrating heat load components at the outer target, (a) (b) for Case-2, (c) (d) for Case-3 and (d) (e) for Case-4. $n_e^{sep} = 2.0 \times 10^{19}$ m^{-3} for all cases. Width of the detachment is shown by arrows.

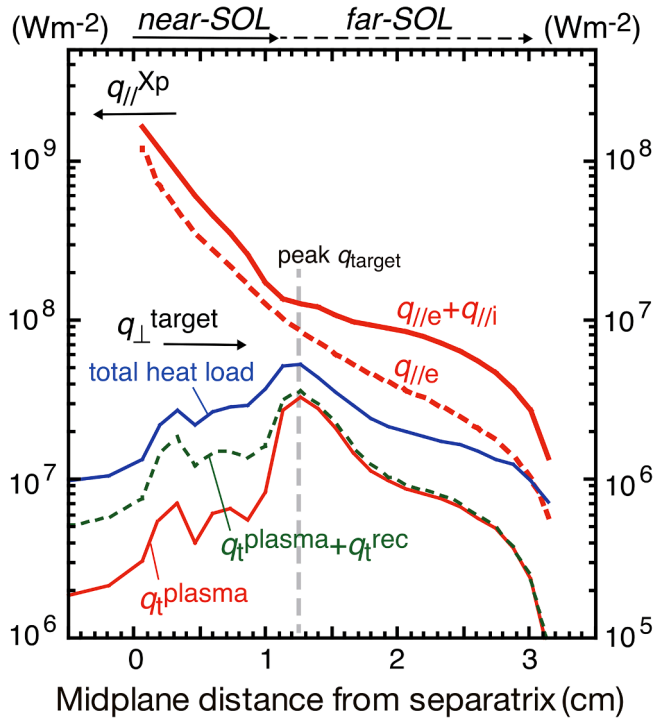

Fig. 5. Profiles of electron and total parallel heat fluxes near the X-point ($q_{//e}^{Xp}$, $q_{//e}^{Xp} + q_{//e}^{Xp}$), and the heat load at the outer target for Case-1 as shown in Fig. 2. Distances from the separatrix at the outer target and near X-point are mapped to the midplane SOL radius. Electron heat flux and total heat flux for $q_{//}^{Xp}$, and profiles of q_t^{plasma}, $q_t^{plasma} + q_t^{rec}$ and total heat load are plotted.

n_e^{div} is decreased to 10^{18}-10^{19} m^{-3}. T_i^{div} becomes larger than T_e^{div} by the factor of 3–4 due to reduction in the energy exchange rate. For Case-3 and Case-4, the total heat load is increased due to the increase in q_t^{plasma}, while q_t^{rad} is slightly reduced.

3.3. Influence of heat flux profile on divertor heat load

Fig. 5 plots profiles of the heat load at the outer target (q_t^{plasma}, $q_t^{plasma} + q_t^{rec}$, total q_{target}) and the electron and total parallel heat fluxes near the X-point ($q_{//e}^{Xp}$ and $q_{//e}^{Xp} + q_{//i}^{Xp}$) for Case-1, mapping to the same r^{mid}. Corresponding width of the partial detachment and radius of the peak q_{target} are ~ 1 cm and 1.25 cm, respectively. Both $q_{//e}^{Xp}$ and $q_{//e}^{Xp} + q_{//i}^{Xp}$ profiles are described by two-exponential function, i.e. $q_{//}(r^{mid}) = q_{//}^{near} exp(-r^{mid}/\lambda_{q//}^{near}) + q_{//}^{far} exp(-r^{mid}/\lambda_{q//}^{far})$. The decay lengths of near-SOL ($\lambda_{q//}^{near}$) and far-SOL ($\lambda_{q//}^{far}$) for the $q_{//e}^{Xp}$ profile, mostly attributed by the electron conduction, correspond to 2.3 and 8.9 mm, respectively. Those for the $q_{//e}^{Xp} + q_{//i}^{Xp}$ profile are 2.9 and 18 mm, which are larger than those for the $q_{//e}^{Xp}$ profile due to contributions of the ion conduction and convection components. The plasma temperatures at the separatrix are high, i.e. $T_e^{sep} = 360$ eV and $T_i^{sep} = 820$ eV, due to large exhaust power and low density compared to ITER. Thus, the $q_{//}$ profile in the SOL becomes narrow, compared to 3.6 mm in ITER simulation result, whereas $\chi_i = \chi_e = 1$ m^{2}s^{-1} and $D = 0.3$ m^{2}s^{-1} are the same values [14].

On the other hand, large $q_{//}$ near the separatrix ($r^{mid} \leq 1$ cm) is significantly reduced in the divertor mostly due to large radiation loss and detachment. The flux surface location of the peak q_{target} ($r^{mid} = 1.25$ cm) corresponds to the boundary of the far-SOL in the $q_{//e}^{Xp} + q_{//i}^{Xp}$ profile, and the peak q_{target} is determined by the local T_e^{div} and T_i^{div}. It is noted that $\lambda_{q//}^{near}$ values for $q_{//e}^{Xp}$ and $q_{//e}^{Xp} + q_{//i}^{Xp}$ profiles of Case-2 are decreased to 1.9 and 2.5 mm, respectively, due to increases in T_e^{sep} and T_i^{sep} with increasing P_{sep}. At the same time, the near-SOL width in the $q_{//e}^{Xp} + q_{//i}^{Xp}$ profile is reduced slightly from 1.1 to 0.9 cm, and the boundary of the far-SOL is shifted towards the separatrix. These characteristics of the total $q_{//}$ profile are further enhanced with increasing $P_{sep} \cdot (1\text{-}f_{rad}^{*div})$, i.e. Case-3 and Case-4. Therefore, the peak q_{target} is increased with decreasing the partial detachment width and increasing the local T_e^{div} and T_i^{div}.

4. Effect of radial diffusion on divertor operation

Radial diffusion of the SOL plasma affects profiles of the heat and particle fluxes. The decay length of the $q_{//}(r^{mid})$ profile near the

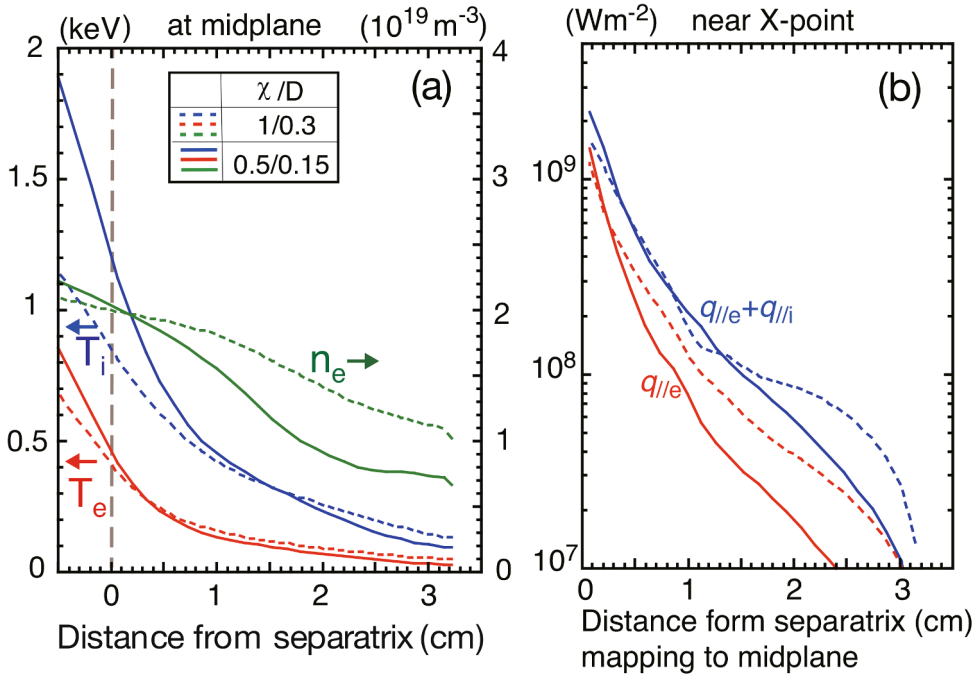

Fig. 6. (a) Profiles of electron and ion temperatures and electron density at the outer midplane for Case-1 and $n_e^{sep} = 2.0 \times 10^{19}$m^{-3}. Solid and dotted lines show results with $\chi = 0.5$ m^{2}s^{-1} and $D = 0.15$ m^{2}s^{-1} and the reference ($\chi = 1$ m^{2}s^{-1} and $D = 0.3$ m^{2}s^{-1}), respectively. (b) Profiles of electron heat flux and total heat flux near X-point. Solid and dotted lines correspond to the smaller and reference χ and D cases, respectively.

separatrix was scaled by $\lambda_{q//}^{Eich} = 0.7 \cdot B_t^{-0.77} \cdot q_{95}^{1.05} \cdot P_{sep}^{0.09}$ [mm, T, MW] [20], based on experiment database of the heat load profile at the outer target under the attached divertor condition. The scaling predicts 0.9 and 1.3 mm for ITER and JA-DEMO, respectively, which are narrower than those calculated in the simulations. Effects of the smaller plasma diffusion on the divertor operation were investigated. Simulations with reducing both χ and D to half values, i.e. $\chi_e = \chi_i = 0.5\ m^2s^{-1}$, $D = 0.15\ m^2s^{-1}$, were performed for the four cases. The plasma temperature and density profiles at the midplane are compared for Case-1 in Fig. 6(a), i.e. solid and dotted lines show results with the smaller χ and D case and the reference case, respectively. It is noted that n_e^{sep} is increased by the reduction of D with the same gas puff rate. In order to compare profiles at the same n_e^{sep} of $2.0 \times 10^{19}\ m^{-3}$, the gas puff rate is reduced to 50 Pam^3s^{-1} for the smaller χ and D case. Radial gradients of T_e, T_i and n_e profiles are increased, and n_e is decreased in the whole SOL region. T_e^{sep} and T_i^{sep} are increased from 360 to 390 eV, and 820 to 1190 eV, respectively, where increase in T_i^{sep} is significant near the separatrix. Solid lines in Fig. 6(b) show the $q_{//e}^{Xp}$ and $q_{//e}^{Xp} + q_{//i}^{Xp}$ profiles for the smaller χ and D case. The radial gradients are increased, and their $\lambda_{q//}^{near}$ are decreased from 2.3 to 1.9 mm and from 2.9 to 2.6 mm, respectively. Here, these are not small enough to simulate the case with the empirical scaling of $\lambda_{q//}^{Eich}$. Their $\lambda_{q//}^{far}$ are also decreased and transition from the near-SOL to far-SOL is rather gradual. At the outer divertor target, Fig. 2(d) and Fig. 7(a) show that the detachment width is decreased from 12 to 7 cm. Fig. 2(f) and Fig. 7 (b) show that the location of the peak q_{target} is shifted from $r^{div} = 15$ to 10 cm, and that the peak is increased from 5.8 to 9.5 MWm^{-2} mostly due to large increases in the local T_e^{div} and T_i^{div}, whereas n_e^{div} is reduced.

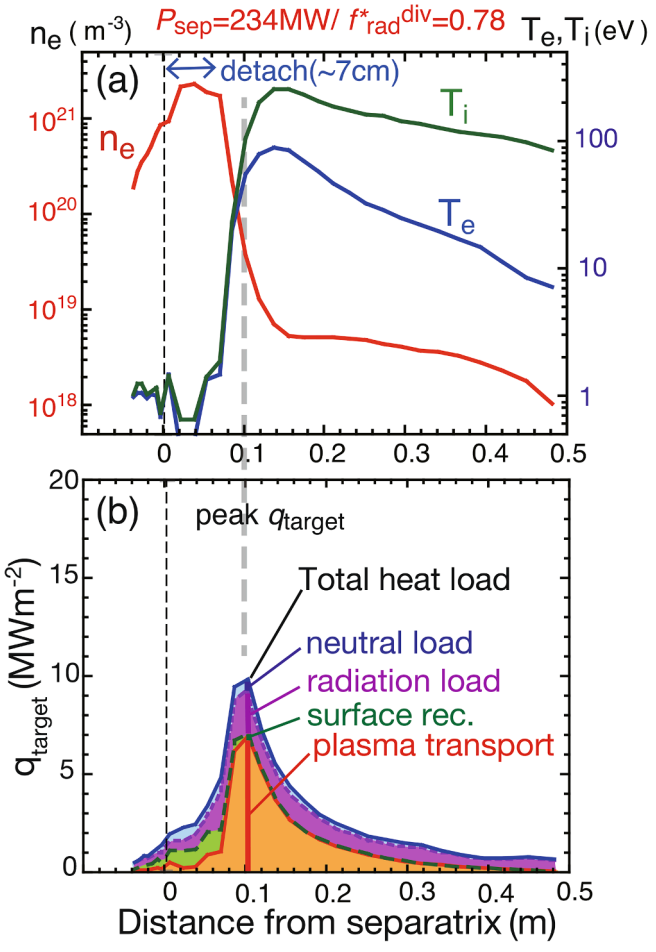

Fig. 7. Profiles of (a) T_e^{div}, T_i^{div}, n_e^{div}, (b) q_{target} and integrating heat load components for Case-1 with $\chi_e = \chi_i = 0.5\ m^2s^{-1}$ and $D = 0.15\ m^2s^{-1}$. Width of the detachment is shown by arrows.

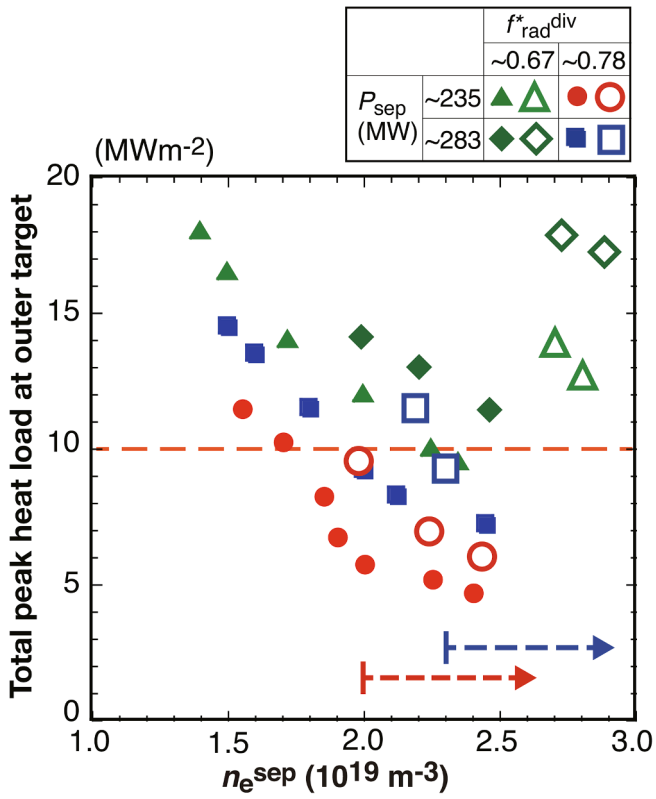

Fig. 8. Results of the peak q_{target} at the outer target for the reference and reduced χ and D cases as a function of n_e^{sep}. Open circles, squares, triangles and diamonds correspond to representative results of the reduced χ and D cases for Case-1, Case-2, Case-3 and Case-4, respectively. Red, and blue dotted lines show n_e^{sep} ranges with peak $q_{target} \leq 10\ MWm^{-2}$ for the reduced χ and D results of Case-1 and Case-2, respectively. (For interpretation of the references to color in this figure legend, the reader is referred to the web version of this article.)

Results of the peak q_{target} at the outer target for the smaller χ and D cases are added by open symbols in Fig. 8. Similar to those in Section 3.2, the peak q_{target} is increased with increasing $P_{sep} \cdot (1\text{-}f^{*div}_{rad})$ and they are reduced with increasing n_e^{sep} for each case. Lower boundary of n_e^{sep} for $q_{target} \leq 10\ MWm^{-2}$ is determined to be 2.0×10^{19} and $2.3 \times 10^{19}\ m^{-3}$ for Case-1 and Case-2, respectively. Therefore, the high f^{*div}_{rad} (~0.78) cases are acceptable in the low n_e^{sep} operation, where higher n_e^{sep} ($\geq 2.3 \times 10^{19}\ m^{-3}$) is required for Case-2. On the other hand, for Case-3 and Case-4, i.e. lower f^{*div}_{rad} (~0.67) cases, the peak q_{target} and n_e^{sep} are significantly increased, thus the divertor operation is difficult in the low n_e^{sep} range. As a result, the reduction in χ and D to half values significantly affected the divertor power exhaust due to increase of the peak $q_{//}$ near the separatrix and reduction of n_e in the outer flux surfaces. In order to produce the detachment plasma at the significantly large $q_{//}$ region and to reduce the peak $q_{target} \leq 10\ MWm^{-2}$, high f^{*div}_{rad} of 0.8 level was necessary for JA-DEMO 2014 and JA-DEMO higher-κ designs.

5. Issues of partial detachment and impurity seeding

Reduction in T_e^{div} and T_i^{div} is an important requirement of the divertor performance in order to reduce the erosion of the W-target in the partial detachment. In particular, in the steady state DEMO, surface erosion by impurity (Ar) ions is anticipated since the ion fluence is expected to be 50–100 times larger than ITER. Closed circles, squares and triangles in Fig. 9 (a) show the maximum T_e^{div} at the attached plasma region for Case-1, Case-2 and Case-3, respectively, and they are decreased significantly with increasing n_e^{sep} due to extending the particle recycling to the outer flux surfaces. For both Case-1 and Case-2, the maximum T_e^{div} is similarly

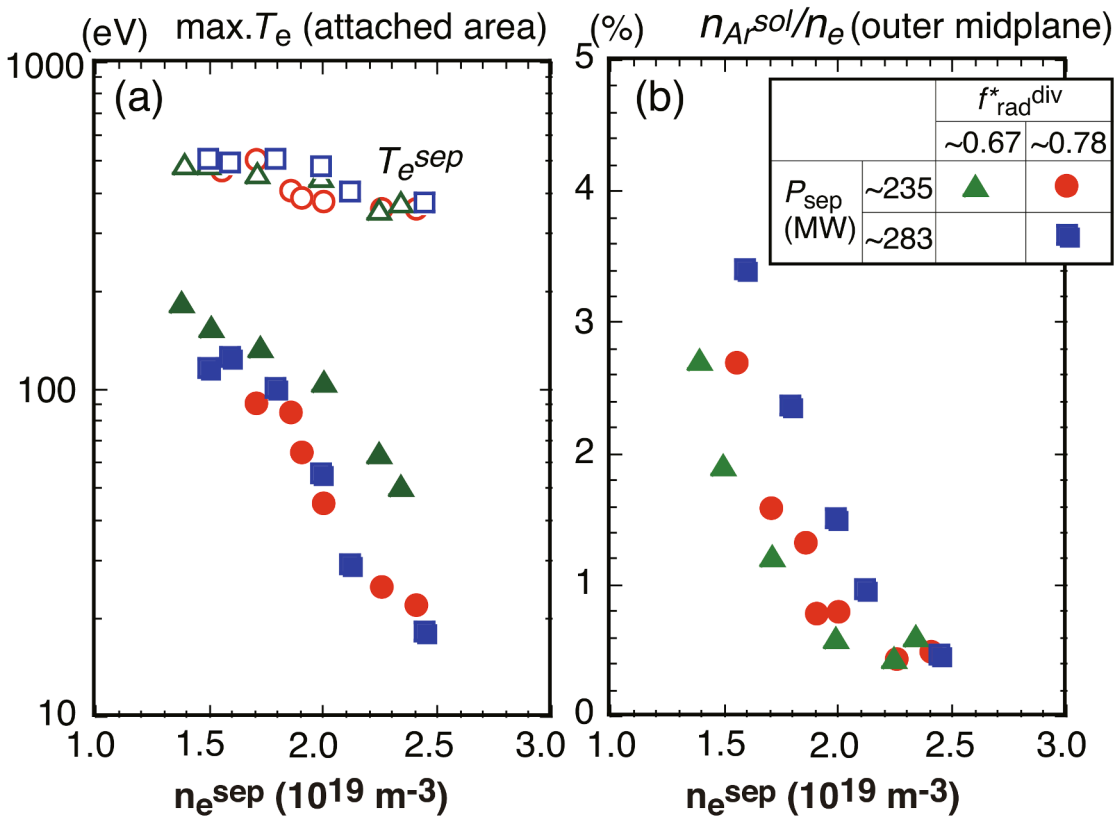

Fig. 9. (a) Maximum T_e^{div} at the attached region of the outer target, and corresponding T_e^{sep} near the separatrix at the midplane. (b) Ar concentration near the separatrix at the midplane SOL as a function of n_e^{sep}. Circles, squares and triangles correspond to Case-1, Case-2 and Case-3, respectively.

decreased to 17–25 eV in the low n_e^{sep} of 2.0–2.5 $\times$ 10^{19} m^{-3}, while it becomes high such as 50–60 eV for Case-3 due to lower f^{*div}_{rad}.

Net erosion (d) is estimated by a simple formula: d(mm) = $10^3 \cdot R_{net} \cdot Y_i \cdot C_i \cdot \Gamma_{i\perp}$(D m^{-2}s^{-1})$\cdot$ 3.15 $\times$ $10^7 t$(year)/[6.02 $\times$ 10^{26}/183.8$\cdot\rho$] = 4.95 $\times$ $10^{-19} R_{net} \cdot Y_i \cdot C_i \cdot \Gamma_i \cdot t$, where R_{net}, Y_i, C_i, Γ_i and ρ are the ratio of net to gross erosion rates, sputter yield by impurity, impurity concentration, incident ion flux and W mass density (19.3 $\times$ 10^3 kgm^{-3}), respectively. R_{net} and $Y_i \cdot C_i$ are critical factors and Y_i is significantly increased with the plasma temperature relevant to the attached plasma condition. For example, assuming R_{net} = 0.1 and using $Y_i \cdot C_i \sim 4 \times 10^{-4}$ for $c_{Ar}^{div} \sim$ 0.2% [21] for the relatively low $T_e^{div} \sim$ 20 eV (at n_e^{sep} = 2.3 $\times$ 10^{19} m^{-3}) and $\Gamma_i \sim 10^{23}$ D m^{-2}s^{-1} in Case-1, d is estimated to be 2.5 mm after a year-long operation, which is a half of the thickness of the monoblock design (5 mm). Therefore, operation at further high n_e^{sep} or sweep of the strike-point location is required even in Case-1 and Case-2. Thus, Case-3 is not acceptable.

Recently, processes of W-erosion, transport and deposition were calculated by IMPGYRO-EDDY code [22], in which kinetic simulation processes include ionization of sputtered W-atom, finite Larmor radius effect on W ion, prompt re-deposition, and kinetic forces on W ions by the plasma $\nabla T_{i//}$ and flow. Under a partial detached plasma condition, W-erosion and deposition were repeated locally in the attached plasma mostly by seeding impurity (Ar), and R_{net} was reduced to 0.01 at low T_e^{div} ($\leq$20 eV) due to the finite Larmor effect and the plasma flow to the divertor target. This result suggests that the target design is acceptable until the scheduled replacement (1–2 years). Self-consistent simulation with the W transport and the determination of R_{net} is required.

In this n_e^{sep} scan, the Ar gas puff rate was decreased with increasing the fuel puff rate in order to maintain f^{*div}_{rad}. While increase of n_{Ar}/n_e above the target (c_{Ar}^{div}) is preferable to enhance the radiation loss in the divertor, n_{Ar}/n_e in SOL (c_{Ar}^{sol}) should be consistent with c_{Ar}^{main} to control P_{rad}^{main} and fuel dilution in the main plasma. Fig. 9 (b) shows c_{Ar}^{sol} at the midplane SOL (near the separatrix), and they are decreased with increasing n_e^{sep}. Here, c_{Ar}^{sol} for Case-2 (higher P_{sep} and larger f^{*div}_{rad}) is large in the low n_e^{sep}, but c_{Ar}^{sol} = 0.4–0.6% is comparable for three cases in the relatively high $n_e^{sep} \geq$ 2.2 $\times$ 10^{19} m^{-3}. Shielding factor of the divertor ($c_{Ar}^{div}/c_{Ar}^{sol}$) is gradually increased from 1.2 to 1.5 to 2.5–3 with increasing n_e^{sep} from 1.5 $\times$ 10^{19} to 2.5 $\times$ 10^{19} m^{-3}. Power exhaust in the main plasma for the JA-DEMO 2014 and JA-DEMO with higher-κ designs requires c_{Ar}^{main} of 0.25% and 0.6%, respectively, which are lower than and comparable to c_{Ar}^{sol} in the simulation results. Further study of experiment and transport modelling inside the separatrix is necessary to determine ratio of $c_{Ar}^{main}/c_{Ar}^{sol}$, which is affected by the H-mode pedestal in the DEMO plasma.

6. Summary

Divertor performance has been investigated for the JA-DEMO design, based on the ITER-like divertor geometry with longer leg length of 1.6 m. The divertor simulation code (SONIC) was used to evaluate the heat load and the detachment plasma for the power exhaust scenarios of JA-DEMO 2014 and JA-DEMO higher-κ designs; the former is a primary DEMO concept with $P_{sep} \sim$ 283 MW, and the latter is a revised proposal with $P_{sep} \sim$ 235 MW. The divertor operation with the peak $q_{target} \leq$ 10 MWm^{-2}, corresponding to the surface temperature of the W target below the recrystallization, was determined in the low n_e^{sep} range of 2–3 $\times$ 10^{19} m^{-3} under severe conditions of reducing $f^{*div}_{rad} = (P_{rad}^{sol} + P_{rad}^{div})/P_{sep}$ and diffusion coefficients (χ and D).

The peak q_{target} at the outer divertor was increased with reduction in the detachment width and increasing local T_e^{div} and T_i^{div} at the attached plasma region, leading to enhancement of the net target erosion. The peak q_{target} for the both reference cases ($f^{*div}_{rad} \sim$ 0.78) was acceptable,

and the revised proposal could furthermore reduce the peak q_{target} and allow enough operation margin. A severe case study of $f^{*div}_{rad} \sim 0.68$ showed that higher n_e^{sep} operations such as larger than 2.6×10^{19} and 2.3×10^{19} m^{-3} were required for the primary concept and revised proposal, respectively, in order to control the peak $q_{target} \leq 10$ MWm^{-2}. Another severe case study of reducing χ and D to the half values showed that the revised proposal could handle the peak q_{target} in the low n_e^{sep} range of 2–3 $\times 10^{19}$ m^{-3}, while high n_e^{sep} operation ($\geq 2.3 \times 10^{19}$ m^{-3}) was required for the primary concept. Furthermore, for the small χ and D case, influence of reducing f^{*div}_{rad} was significantly seen in both the peak q_{target} and n_e^{sep}, and it was found that $q_{target} \geq 10$ MWm^{-2} in the low n_e^{sep} range of 2–3 $\times 10^{19}$ m^{-3}.

The large power exhaust scenario in the main plasma and divertor by the radiative cooling is necessary for the DEMO divertor design, and the power exhaust in the main plasma significantly affect the divertor design. The proposed divertor geometry and reference operation parameters (P_{sep}, f^{*}_{rad}, χ, D and n_e^{sep}) were so far consistent with the primary concept and revised proposal of JA-DEMO design. The power exhaust scenario of JA-DEMO with higher-κ and increasing impurity seeding ($f^{main}_{rad} = 0.41$, $P_{sep} = 258$ MW and $P_{sep}/R_p = 30$ MWm^{-1}, estimated by system code) has advantages for the low n_e^{sep} range and enough margin for the divertor operation, compared to the primary JA-DEMO concept ($f^{main}_{rad} = 0.22$, $P_{sep} = 294$ MW and $P_{sep}/R_p = 35$ MWm^{-1}). Further improvements of the divertor geometry and operation options such as different seeding impurity will be investigated in order to extend the partial detachment width and to reduce local T_e^{div} and T_i^{div} at the attached plasma region as well as the peak q_{target}. At the same time, profiles of the diffusion coefficients over the near- and far-SOLs are demanded in order to determine the divertor operation for the DEMO design.

CRediT authorship contribution statement

N. Asakura: Conceptualization, Software, Formal analysis, Investigation, Writing - original draft. **K. Hoshino:** Software, Methodology, Writing - review & editing. **Y. Homma:** Software, Writing - review & editing. **Y. Sakamoto:** Project administration, Resources, Funding acquisition. **:** .

Declaration of Competing Interest

The authors declare that they have no known competing financial interests or personal relationships that could have appeared to influence the work reported in this paper.

Acknowledgments

This work was carried out within the framework of the Broader Approach DEMO Design Activity, using the JFRS-1 supercomputer system at CSC, IFERC, Rokkasho.

References

[1] Y. Sakamoto, et al., DEMO Concept Development and Assessment of Relevant Technologies. 25th IAEA Int. Conf. on Fusion Energy (St. Petersburg, Russia, 2014) FIP/3-2Rb, https://www-naweb.iaea.org/napc/physics/FEC/FEC2014/fec2014-preprints/222_FIP34Rb.pdf.
[2] K. Tobita, et al., Fusion Sci. Technol. 72 (2017) 537.
[3] M. Nakamura, et al., Fusion Eng. Des. 87 (2012) 864.
[4] N. Asakura, et al., Nucl. Fusion 57 (2017), 126050.
[5] R. Wenninger, et al., Nucl. Fusion 57 (2017), 016011.
[6] M. Siccinio, et al., Nucl. Fusion 59 (2019), 106026.
[7] G. Zhuang, et al., Nucl. Fusion 59 (2019), 112010.
[8] S. Kwon, et al., Fusion Eng. Des. 159 (2019), 111770.
[9] R.A. Pitts, et al., Nucl. Mater. Energy. 20 (2019), 100696.
[10] N. Asakura, Recent Developments of Plasma Exhaust and Divertor Design for Tokamak DEMO Reactors. 14th Int. Sym. on Fusion Nuclear Tech. (Budapest, Hungary, 2019) PL-7.
[11] K. Shimizu, et al., J. Nucl. Mater. 313–316 (2003) 1277.
[12] H. Kawashima, et al., J. Plasma Fusion Res. 1 (2006) 31.
[13] K. Hoshino, et al., J. Nucl. Mater. 463 (2015) 573.
[14] A. Kukushkin, et al., J. Nucl. Mater. 438 (2013) S203.
[15] N. Asakura, et al., Fusion Eng. Des. 136 (2018) 1214.
[16] A. Kallenbach, et al., J. Nucl. Mater. 337–339 (2005) 381.
[17] A.W. Leonard, et al., Nucl. Fusion 57 (2017), 086033.
[18] T. Eich, et al., Nucl. Fusion 58 (2018), 034001.
[19] M. Groth, et al., Nucl. Fusion 53 (2013), 093016.
[20] T. Eich, et al., Nucl. Fusion 53 (2013), 093031.
[21] A. Kallenbach, et al., Plasma Phys. Contl. Fus. 47 (2005) B202.
[22] Y. Homma, et al., Nucl. Mater. Energy. 122 (2017) 323.